Noname manuscript No.
(will be inserted by the editor)

Vertical Wave Coupling in the Low-Latitude Ionosphere-Thermosphere as revealed by Concurrent ICON and COSMIC-2 Observations

Federico Gasperini · Geoffrey Crowley · Thomas J. Immel · Brian J. Harding

Received: date / Accepted: date

Abstract It is now well established that waves generated in the lower atmosphere can propagate upward and significantly impact the dynamics and mean state of the ionosphere-thermosphere (IT, 100-600 km) system. Given the geometry of magnetic field lines near the equator, a significant fraction of this IT coupling occurs at low latitudes (<30°) and is driven by global-scale waves of tropical tropospheric origin, such as the diurnal eastward-propagating tide with zonal wavenumber 3 (DE3) and the ultra-fast Kelvin wave (UFKW). Despite recent progress, lack of coincident global observations has thus far precluded full characterization of the sources of day-to-day variability of these waves, including nonlinear interactions, and impacts on the low-latitude IT. In this work, in-situ ion densities from Ionospheric Connection Explorer (ICON)'s and Constellation Observing System for Meteorology, Ionosphere and Climate 2 (COSMIC-2)'s Ion Velocity Meter (IVM) along with remotely-sensed zonal winds from ICON's Michelson Interferometer for Global High-resolution Thermospheric Imaging (MIGHTI) are used to reveal a rich spectrum of waves coupling the lower (∼90-105 km) and middle (∼200-270 km) thermosphere with the upper F-region (∼540 and ∼590 km) ionosphere. Spectral analyses for a 40-day period of similar local time demonstrate prominent IT coupling via DE3, a 3-day UFKW, and the two ∼1.43-day and ∼0.77-day secondary waves from their nonlinear interactions. While all these waves are found to dominate the F-region spectra, only the UFKW and the 1.43-day secondary wave can propagate to ∼270 km suggesting E-region wind dynamo processes as major contributors to their observed ionospheric signatures.

Keywords Ionosphere · Thermosphere · Wave Coupling · ICON · COSMIC-2

F. Gasperini, G. Crowley
Atmospheric and Space Technology Research Associates, LLC, Louisville, CO, USA
E-mail: fgasperini@astraspace.net

T. J. Immel, B. J. Harding
Space Sciences Laboratory, University of California, Berkeley, CA, USA

1 Introduction

The extent to which terrestrial weather can influence the dynamics and mean state of the ionosphere-thermosphere (IT, 100-600 km altitude) is an important discovery of the last two decades or so. Much of this coupling occurs at low latitudes (<30°), due to the geometry of magnetic field lines near the equator, and is driven by waves that are excited by deep convective processes in the tropical troposphere and that propagate upwards into the IT system. Tropical troposphere variability is essentially mapped into the IT system through a variety of neutral-ion coupling processes, and over a range of spatial and temporal scales (e.g., Liu et al., 2016; Yigit and Medvedev, 2015).

It is now well established that few waves from the tropical wave spectrum (hereafter 'ultra-fast tropical waves', or UFTWs) preferentially propagate into the IT system, and modify neutral density and satellite drag (Forbes et al., 2009; Oberheide et al., 2009; Gasperini et al, 2015, 2018), thermospheric winds (Gasperini et al., 2015, 2020), ionospheric densities (Chang et al., 2011; He et al., 2011; Gu et al., 2014a; Pedatella and Forbes, 2009; Gasperini et al., 2021), and even GPS scintillations (Liu et al., 2013) to an important degree. Two of the more prominent and well-established UFTW are the eastward-propagating diurnal tide with zonal wave number s = -3 (DE3), and the eastward-propagating ∼2.5-day to ∼4-day period ultra-fast Kelvin wave with zonal wave number s = -1 (UFKW, or UFKW1). DE3 is believed to originate primarily in the tropical troposphere by latent heat release in deep convective clouds (e.g., Hagan, 1996; Lieberman et al., 2007), and its equatorially symmetric mode, which is the largest component in the lower thermosphere (Truskowski et al., 2014), is well capable of propagating into the middle thermosphere (Oberheide et al., 2011a; Gasperini et al., 2015, 2018) and ionosphere (Gasperini et al., 2021) due to its long vertical wavelength of ∼56 km. UFKWs are a special kind of gravity waves modified by the Earth's rotation and trapped in the equatorial and low-latitude regions, where the Coriolis force is negligible (Salby et al., 1984; Andrews et al., 1987). UFKWs originate primarily from latent heat release in the tropical troposphere and have predominance of the kinetic energy in the zonal wind component. UFKWs have the longest vertical wavelength (>50 km) of all Kelvin waves and thus can penetrate well into the lower and middle thermosphere, with amplitudes of ∼25 K in temperature and ∼30 m/s in zonal wind around 110 km (Gu et al., 2014a), and zonal wind amplitudes exceeding 10 m/s near 260 km (Gasperini et al., 2015). In the context of this study, lower thermosphere denotes altitudes extending from ∼90-120 km and middle thermosphere refers to altitudes ranging between ∼120-270 km.

The ionospheric plasma distribution and dynamics in the equatorial and low-latitude regions are primarily controlled by E-region and F-region electrodynamic processes (e.g., Fejer, 1981, 2002; Heelis, 2004; England et al., 2011). In particular, the dynamo wind modulation induced by various waves in the ionospheric E-region is commonly used to interpret ionospheric variability associated with UFTW-induced changes in the thermosphere. Additionally,

as discussed above, UFTWs with sufficiently large vertical wavelengths (e.g., greater than ∼60 km) are capable of propagating into the middle thermosphere causing UFTW-like oscillations in the F-region dynamo electric fields, ion densities, and ion drift velocities. Moreover, UFTWs can lead to an overall depletion of the mean ionospheric electron/ion density due to the so-called mixing effect, caused by an additional residual circulation that leads to a net vertical transport and diffusion of atomic oxygen and molecular nitrogen (Yue and Wang, 2014; Jones et al., 2014). Lastly, different components of the wave spectrum can interact with each other to produce secondary waves (SWs) that propagate from their sources as independent waves (Palo et al., 1999; Moudden and Forbes, 2013, 2014; Gasperini et al., 2014, 2015, 2017a, 2018; Yamazaki et al., 2021; Forbes et al., 2021a,b). As the SWs occur with wave periods and zonal wave numbers different than the primary interacting waves, the aggregation of primary waves and SWs results in significant more spatial and temporal variability than that from the simple linear superposition of the primary waves (Gasperini et al., 2015; Forbes et al., 2021b). A number of studies demonstrated that the aforementioned UFTWs and the SWs arising from their nonlinear interactions play key roles in driving day-to-day and intra-seasonal variability in the IT system (Egito et al., 2018; Gasperini et al., 2015, 2017, 2020, 2021; Gan et al., 2017; Gu et al., 2018; Miyoshi and Yamazaki, 2020; Triplett et al., 2019; Forbes et al., 2021a,b; Liu et al., 2021). Previous modeling work by Gasperini et al. (2017a) showed that SWs arising from UFTW interactions are mainly excited below ∼100 km, and that their exponential growth with height combined with molecular dissipation leads to SW amplitude maxima around ∼110-140 km and significant amplitudes that are still present near 260 km. SWs are thus capable of carrying longer periodicities, such as those of UFKWs and planetary waves, into the F-region ionosphere either through E-region dynamo processes (Miyoshi and Yamazaki, 2020), or via direct propagation into the F-region (England et al., 2010, 2011; Forbes et al., 2018; Forbes, Maute and Zhang, 2020a,b,c).

Despite this important process achieved in the past decade or so, our current understanding of the IT coupling involving large-scale waves is primarily based on general circulation model (GCM) simulations. This is largely because of lack of coincident global observations of the physical parameters responsible for IT coupling. In particular, significant uncertainty still exists on the relative contribution between E-region and F-region electrodynamic processes in contributing ionospheric variability. Fully charactering the UFKW amplitude and phase spectrum in concurrent lower and middle thermosphere winds and F-region ion density holds the promise to significant advance our understanding in this area.

Recent availability of concurrent Ionospheric Connection Explorer (ICON) and Constellation Observing System for Meteorology, Ionosphere and Climate 2 (COSMIC-2) satellite observations during the solar minimum and geomagnetically-quiescent years of 2020 and 2021 provides the unique opportunity to develop a comprehensive understanding of how UFTW and their nonlinear interactions couple different regions of the IT system. In this work,

we employ contemporaneous in-situ-measured total ion densities from nearly identical Ion Velocity Meter (IVM) instruments onboard ICON and COSMIC-2 (near 590 and 540 km, respectively) and remotely-sensed zonal winds from ICON's Michelson Interferometer for Global High-resolution Thermospheric Imaging (MIGHTI) instrument (near 90-300 km), along with a so-called pseudo-longitude (PL) spectral analysis method (discussed in detail in Section 3), to provide new insights on the ability of this selected group of high-impact waves to couple lower and middle thermospheric variability with F-region ionospheric variability. The results herein presented focus on the 40-day period between 11 July 2020 and 20 August 2020 when both ICON and COSMIC-2 E2 (C2E2, one the six satellites of the constellation, see discussion in Section 2.2) provided similar (within ±30-min) magnetic local time (MLT) coverage.

The outline of this study is as follows: Section 2 describes the data sets and inter-comparison/validation analyses; Section 3 details the aforementioned PL method; Section 4 contains results from PL spectral analyses; while Section 5 provides a brief summary that includes a statement on the need for further work.

2 Data

This work employs total ion densities measured by ICON IVM (Heelis et al., 2017) and COSMIC-2 IVM (Schreiner et al., 2020), as well as zonal neutral winds from the ICON MIGHTI (Englert et al., 2015, 2017; Harding et al., 2017) during 1 July 2020 - 20 August 2020. Figure 1 shows the time series of the daily F10.7cm solar radio flux (panel *a*) and 3-hourly *kp* geomagnetic (panel *b*) indices during the 40-day period herein analyzed. As illustrated by Figure 1, this period is characterized by low geomagnetic activity (kp<4) and quiet solar flux conditions (68<F10.7<75) making it an excellent period for investigating IT coupling via upward-propagating waves.

2.1 ICON MIGHTI Wind and IVM Ion Density

ICON is a NASA Heliophysics System Observatory mission launched on 10 October 2019 in a nearly circular orbit at an altitude near 590 km with ∼27° inclination to directly measure the processes of ionospheric modification by the dynamics of the neutral atmosphere (Immel et al., 2018, 2019, 2021). This study employs MIGHTI L2-2 V4 green-line vector winds (95-106 km, daytime and nighttime) and MIGHTI L2-2 V4 red-line vector winds (200-270 km, daytime and nighttime). Recent work by Dhadly et al. (2021) demonstrates agreement between MIGHTI and Thermosphere, Ionosphere, Mesosphere Energetics and Dynamics Doppler Interferometer (TIMED/TIDI) zonal wind observations, with correlations around 0.6 and root mean square (RMS) differences of ∼56 m/s, and similar large amplitude longitudinal variations. RMS differences of MIGHTI winds to ground-based radars and interferometers are

on the order of 20 m/s (Harding et al., 2021; Makela et al., 2021). Previous work on TIMED/TIDI by Oberheide et al. (2006) demonstrates that such errors are negligible in tidal/wave fits when a sufficiently large number of profiles are used. This study further employs ICON IVM-A L2-7 V5 total ion density measurements (Heelis et al., 2017; Huba et al., 2021; Park et al., 2021a,b). The IVM data are down-selected by including data only for times where the two 'RPA' and 'DM' flags are both equal to zero. As noted by Heelis et al. (2017), ICON ion density are generally always reliable and with accuracy exceeding 10^3 cm^{-3}. See the Acknowledgments for a statement on data availability.

2.2 COSMIC-2 IVM Ion Density

The COSMIC-2 satellite mission consisting of six low-Earth-orbit satellites (C2E1-C2E6) was launched on 25 June 2019 into a nearly circular ∼720 km altitude orbit at an inclination of ∼24° (Schreiner et al., 2020). After over one year in orbit, C2E1-C2E6 reached their final orbital configuration near 540 km with a ∼60° longitude separation (Lin et al., 2020; Chou et al., 2021). C2E1-C2E6 provide in-situ measurements of ion densities from onboard IVM instruments similar in design to the IVM instrument onboard ICON. C2E1-C2E6 ion density uncertainties are estimated to be around 3x10^3 cm^{-3} (Chou et al., 2021). For this study we employ the L2 post-processed total ion density data product from C2E2. See the Acknowledgments for a statement on data availability.

2.3 Comparative Analyses and Inter-Validation of ICON and C2E2 IVM

As previously noted, during 11 July 2020 - 20 August 2020 ICON and C2E2 offered similar MLT coverage from orbits separated in altitude by only about 50 km. This arrangement provides an excellent opportunity to perform detailed correlative analyses on these data sets. Figure 2a shows the time series of C2E2 (blue line) and ICON (red line) equatorial MLT during 1 August 2019 through 23 March 2021, while Figure 2b shows the corresponding equatorial mean altitudes. A full diurnal cycle (24-hr of MLT) is completed in about 1 month for both ICON and C2E2 near the equator. C2C2 was lowered from its initial altitude near 720 km to its final ∼540 km orbital configuration in March 2020, while ICON was launched and operates near 590 km altitude. As shown in Figure 2a, during this 40-day period equatorial ICON and C2E2 IVM measurements are within ±30-min of MLT.

In order to investigate the degree of agreement between the ICON and C2E2 IVM ion density data prior to applying spectral analysis methods, we performed correlation analyses between these datasets during the 40-day period of similar MLT noted above. Figures 3a and 3b show the equatorial ICON (red dots) and C2E2 (blue dots) MLT and mean altitude, respectively; while Figures 3c and 3d show ICON and C2E2 equatorial total ion densities during

daytime (6-18 MLT) and nighttime (0-6 MLT and 18-24 MLT), respectively. Ion density values up to ∼2.8x10^5 during daytime and ∼1.8x10^5 during nighttime are found for both ICON and C2E2. The 24-hour local time (LT) precession cycle of about 30 days for ICON and C2E2 IVM is evident in Figure 3a. ICON and C2E2 ion densities display remarkable agreement, with similar temporal variability. The Pearson correlation coefficient between the two time series is r=0.91 during daytime and r=0.87 during nighttime. The not perfect agreement between the ICON and C2E2 IVM measurements can be ascribed to geophysical variability in the data between about 540 km and 590 km, small differences in MLT sampling, and uncertainties in the ICON and C2E2 ion density retrievals.

Further comparisons between the ICON and C2E2 total ion densities during 11 July 2020 and 20 August 2020 are provided in Figure 4. Panels 4a-l contain scatter plots of ICON and C2E2 ion density, with daytime and nighttime data combined, at different magnetic latitudes (MLAT) from 27°S to 28°N in 5° steps. Pearson correlation coefficients are found to vary between r=0.631 and r=0.785, with higher correlations between 13°N and 28°N MLAT. Stronger correlation are generally found for MLAT sectors containing the largest amount of data (i.e., 12°S-18°N), with data near 17°S and 28°N as notable exceptions (Figure 4m). Figure 4n contains the line plot of Pearson correlation coefficients as a function of MLAT during daytime (blue line) and nighttime (red line), which demonstrates higher daytime (nighttime) correlations for MLAT <0° (>0°). It would be beyond the purview of the current study to investigate the origin of the differences and their relation to MLAT and MLT. Note that while some dependencies on MLAT and MLT in the correlations are present, within about -20°<MLAT<20° the correlations are always greater than 0.6. These findings provide reassurance in the quality of the low-latitude C2E2 and ICON IVM L2 total ion density products during the 40-day period herein employed.

3 Methods

3.1 Ascending-Descending Node Differences

Due to their slow LT precession, analyses of ICON's and C2E2's data for investigating large-scale wave variability proves challenging. This is because the waves derived using the full ∼30-day precession cycle are an average over this period and changes in the zonal mean are viewed as a LT variation. Thus the evolution of the zonal mean can alias into the derived migrating tidal fields and temporal variations in stationary and long-period planetary waves can alias into the non-migrating tidal retrievals. See discussions in Zhang et al. (2006), Forbes and Wu (2006), and Gasperini et al. (2015, 2017b) for further details. Various methods of analyzing slowly-precessing satellite data to infer tidal and wave information have been used to improve these effects. Notable studies by Lieberman (1991) and Oberheide and Gusev (2002) estimated diurnal

tides on a daily basis by taking differences between ascending and descending node (hereafter 'ADND') measurements that are 12 hours or less apart in LT. This method eliminates aliasing due to long-term trends and semidiurnal tidal variability, but ambiguities in zonal wave number can occur, especially for westward propagating tides. As explained in Section 4, we take advantage of this ADND method to facilitate the interpretation of our spectral analysis results.

3.2 Pseudo-Longitude Spectral Method

A pseudo-longitude (PL) spectral method developed by Moudden and Forbes (2010, 2011, 2013, 2014) was employed by Gasperini et al. (2015, 2017a, 2018) to investigate wave-wave interactions from slowly-precessing TIMED Sounding of the Atmosphere using Broadband Emission Radiometry (SABER) and Gravity Field and Steady-State Ocean Circulation Explorer (GOCE) satellite observations. As briefly described below, we apply this PL method to ICON and C2E2 data. More detailed discussions on the PL method can be found in the seminal works by Moudden and Forbes (2010, 2011).

The methodology consists of ordering data in PL, λ_p, defined as λ_p=|λ - c x 2π|, where c is the number of times all longitudes (λ) have been covered by a slowly precessing low-Earth orbiting satellite. This arrangement eliminates the fictitious discontinuity at 2π longitude. If the mathematical description of a $n\Omega$-frequency tide with zonal wave number s is $cos(n\Omega t + s\lambda_p)$ and that of a longer $\delta\Omega$-frequency wave with zonal wave number m is $cos(\delta\Omega t + m\lambda_p)$, their interaction yields SWs with frequencies equal to $\Omega(n \pm \delta)$ and zonal wave numbers equal to $s \pm m$.

When sampled at a nearly constant LT, a tide appears as a wave in the form $cos(n\Omega t_{LT}+(s-n)\lambda_p)$, a UFKW in the form $cos(\delta\Omega t_{LT}+(m-\delta)\lambda_p)$, and their sidebands in the form $cos[(n \pm \delta)\Omega t_{LT} + (s \pm m - n \mp \delta)\lambda_p]$. As noted in Section 1, the various zonal wave numbers contribute to the zonal variability in any atmospheric field. Spectral analysis of a given time series of space-based measurements, can reveal the dominant values of $(s - n)$, $(m - \delta)$ and $(s \pm m - n \mp \delta)$, and subsequently the dominant tides, UFKW, and any UFKW-tide modulations. In the above representations, tides appear as integers, and differentiating between a UFKW and the UFKW modulation of a migrating tide ($s - n = 0$) is not possible.

As the LTs of both ICON and C2E2 evolve linearly with time, i.e., $t_{LT} = \alpha t + \beta$ with α and β constants (Forbes et al., 2017; Cullens et al., 2020). Using the definition of LT, $t_{LT} = t_{UT} + \lambda_p/\Omega$ (where t_{UT} is universal time), it can be easily shown that the traditional writing of a tidal component may be expressed as: $cos[n\Omega\beta/(1-\alpha) + (s-n)/(1-\alpha)\lambda_p)]$. Thus, spectral analysis will yield the $(s-n)/(1-\alpha)$ wave numbers for tides, $(m-\delta)/(1-\alpha)$ for a UFKW and $((s \pm m) - (n \pm \delta))/(1-\alpha)$ for SWs. Given that α is less than 0.0125 for both ICON and C2E2, their precession is slow enough that the shift it introduces in the spectra is negligible.

A view of the MLAT-PL structure of ICON and C2E2 total ion densities for the ascending and descending portions of the orbit is offered by Figure 5. The large ion density enhancements around 10-25 x 360° (25-40 x 360°) for the descending (ascending) parts of the orbits occur when the MLT is near the afternoon peak in electron density.

4 Spectral Analyses of F-region Ion Densities

As noted in Section 3.1, methods have been developed and applied to estimate diurnal tides on a daily basis by taking ADND from slowly-precessing satellite measurements that are about 12 hours apart in LT (Lieberman, 1991; Oberheide and Gusev, 2002, Gasperini et al., 2015, 2021). In order to eliminate aliasing due to long-term trends, minimize zonal mean and semidiurnal tidal influences, and concentrate on diurnal tidal variability, sets of ADND are first calculated for different latitude sectors (in 5° MLAT bins) from ICON and C2E2 IVM data during 11 July 2020 - 20 August 2020, and subsequently PL spectral method are applied to these ADND sets. Similar to Gasperini et al. (2015), a threshold of at least 9-hour of LT separation between the ascending and descending nodes is used for the wave analyses herein implemented. This requirement constrains the geographic latitude range for spectral analyses to $\sim \pm 10°$ for IVM and to ∼5°N-25°N for MIGHTI.

Figures 6a and 6b show the MLAT-PL structure of ICON and C2E2 ion density ADND near ±30° MLAT. The large ∼30-day variations displaying minima of around -1e5 n/cc near 10-20 x 360° and maxima of around 1e5 n/cc near 30-40 x 360° are due to ICON's and C2E2's ∼30-day-long precession cycles. Spectral analysis results of the PL series in Figures 6a and 6b, calculated averaging ICON and C2E2 data near ±10° MLAT during 1-7 August 2020, are shown in Figures 6c and 6d, respectively. The length of the window is chosen to balance the need to capture longer period waves (e.g., up to 2 cycles for a 3.5-day UFKW), while allowing the approximation of a constant LT. Note that on average for latitudes within ±15° ICON and C2E2 observe a 24-hour LT precession in about 41 days (see Figure 4a in Cullens et al. (2020) for ICON's LT precession); thus low-latitude ICON and C2E2 data averaged over a 7-day period observe a LT change of about 4.1 hours. The spectra are obtained using least squares methods (Vanicek, 1969, 1971), which are more adaptable than the Fourier transform for non-uniformly spaced and gapped data. The horizontal line in every spectrum plot indicates a critical percentage variance at a 95% confidence level for detecting significant peaks in the spectrum.

Remarkable agreement exists between the ICON and C2E2 ion density PL spectra. Clearly evident in both spectra are peaks around 1, 2, 3 and 4 cycles. As discussed in detail in Section 3.1, in a PL spectrum non-migrating tidal peaks appear at integers while migrating tides are not observable. The x-axis represents the frequency in number of cycles per 360° in PL and the y-axis is the power. The major peaks correspond to integer values which directly points to tides: among all possible values of $| s-n |$, $| m-\delta |$ and $| (s \pm m)-(n \mp \delta) |$

only $\mid s-n \mid$ are integers. The abbreviated name of the diurnal and semidiurnal tides potentially responsible for the observed integer peaks are indicated in Figures 6c and 6d. D stands for diurnal, S for semidiurnal, E and W for eastward and westward propagating tides, respectively. Each abbreviated name ends with the zonal wave number. As the PL spectra are calculated on ADND, the semidiurnal tidal signatures are largely absent from Figures 6c and 6d. The migrating tides are not distinguishable from the mean since $s - n = 0$. Based on previous studies (e.g., Truskowski, 2014) most westward propagating and terdiurnal tides can be assumed to be of smaller amplitude although they do contribute to each peak.

Particular prominent in both ICON and C2E2 spectra are peaks around 2 and 4 cycles marked with green and red 'Δ' symbols, respectively. The peak at 2 cycles can be ascribed to a prominent low-latitude DE1 (with possible minor contributions by TW1 and DW3), while the peak at 4 cycles is evidence of a large DE3 (and possible minor contributions by TE1 and DW5). The presence of a strong DE3 tidal variation in F-region ion density is not unexpected for the early August 2020 period and is in agreement with the well-known seasonal variation of this tidal component excited in the tropical troposphere. The lower and middle thermospheric DE3 is known to maximize around the August-September months (Oberheide et al., 2011a, Gasperini et al., 2017), and the results by Gasperini et al. (2021) already demonstrated prominent F-region ion density DE3 amplitudes during the August-September 2020 period using ICON and Scintillation Observations and Response of The Ionosphere to Electrodynamics (SORTIE) IVM (Crowley et al., 2016) observations.

Also present in the spectra are large periodicities around 1.33 (blue 'Δ'), 0.67 (green '$-$'), 1.0 (orange 'Δ'), 1.67 (brown '$-$'), 2.2 (black '?'), 2.67 (red '$-$'), 3.0 (brown 'Δ'), 3.33 (green '+'), 4.2 (black '?'), 5.33 (red '+') cycles. The power associated with all of these periodicities is higher (and in many cases significantly higher) than the 95% confidence level, denoted by the horizontal dashed lines. The peak near 1.33 cycles is consistent with the signature of a 3-day (i.e., $\delta = 0.33$) UFKW with m = -1 (δ - m = 0.33 - (-1) = 1.33), the peak at 1 cycle can be ascribed to a large D0 (with possible minor contributions from TW2 and DW2), the one at 3 cycles is likely due to DE2 (with possible minor contributions from T0 and DW4), while those at 0.67, 1.67, 2.67, 3.33, and 5.33 cycles are likely the signature of SWs associated with the nonlinear interaction of tides with the 3-day UFKW (color-coded according to the particular tide likely involved in the interaction). Previous studies demonstrated the existence of large quasi-3-day UFKW signatures in the low latitude lower and middle thermosphere density and neutral winds (Gasperini et al., 2015, 2017, 2020) and ionospheric Total Electron Content (TEC, Gu et al., 2014a). Particularly prominent are the SW periodicities near 2.67 and 5.33 cycles associated with DE3-UFKW interactions (red '$-$' and '+' symbols). Based on the discussion in Section 3.2, the SW near 2.67 (5.33) cycles is characterized by zonal wave number -2 (-4) and frequency 0.67Ω (1.33Ω), i.e., period of about 1.5 days (0.75 days). The peaks near 2.2 and 4.2 cycles (denoted with black '?' symbols) are consistent with the interaction of non-migrating tides with a westward-

propagating ∼6-day period wave, e.g., a quasi-6-day wave (Q6DW, Gu et al., 2014b; Gan et al., 2016, 2017, Forbes and Zhang, 2017). Further work would be needed to fully characterize these nonlinear interactions possibly involving Q6DW activity. These efforts are left for a follow-on study.

While Figure 6 demonstrates remarkable agreement between the ICON and C2E2 ion density time series during 11 July 2020 - 20 August 2020 (r=0.91 at the magnetic equator, i.e., >82% of the variance) and their PL spectra during 1-7 August 2020, some differences are worth noting. For instance, detailed comparisons of Figures 6c and 6d reveal a smaller peak at 1 cycles for C2E2 compared to ICON and a smaller UFKW-DE2 sideband at 1.67 cycles for ICON compared to C2E2. These differences are not surprising and are ascribable to additional complexities possibly introduced by (among other effects) wave dissipation, the presence of zonal mean winds, possible in-situ wave-wave interactions, LT sampling differences, and inherent transience.

5 Spectral Analyses of Lower and Middle Thermospheric Winds

Next, the focus is on elucidating the extent to which the F-region ion density wave variations observed by ICON and C2E2 can be traced to lower (∼97-105 km) and middle (∼220-270 km) thermospheric zonal wind variability. To this end, ICON's MIGHTI zonal winds measured during 1-13 August 2020 are analyzed using the PL spectral method detailed in Section 3.2. Figure 7 contains the geographic latitude (10°S-30°N) versus PL series of ADND zonal winds near 270 km (panel a), 220 km (panel b), 105 km (panel c), and 97 km (panel d) and their respective PL spectra calculated at 5°N latitude during 1-7 August 2020 (panels a'-d', respectively). This 7-day period for the PL spectra is selected to be consistent with the ion density results shown in Figures 6c and 6d. The ADND zonal winds exhibit significant differences in their latitude-temporal structures among the various altitudes examined, particularly between 97 km and 105 km. This finding is indicative of large vertical wind shears in this region (e.g., Yamazaki et al., 2022; Englert et al., 2022). The low-latitude ADND zonal winds are found to vary between about -100 m/s and 50 m/s near 97 km and -50 m/s and 150 m/s near 270 km.

The PL spectra contained in Figures 7a'-d' reveal a clear picture of the most prominent large-scale waves present in the lower and middle thermospheric zonal wind during 1-7 August 2020. A remarkable agreement is found with the upper F-region ion density spectra shown in Figures 6c and 6d. Clearly marked in the spectra are peaks around 1.33 cycles due to the 3-day UFKW (blue Δ symbols), 4 cycles due to DE3 (red Δ symbols), as well as peaks near 2.67 (red '$-$' symbols) and 5.33 (red '+' symbols) cycles associated with the two SWs originating from DE3-UFKW interactions. From Figures 7c$'$ and 7d$'$ one can see that the DE3 peak at 4 cycles is more prominent near 105 km than around 97 km. This result is consistent with the vertical propagation and grown of this tidal component known to reach maxima in the ∼110-120 km altitude region. While still present near 220 km with reduced amplitudes,

the thermospheric zonal wind DE3 variability is largely absent near 270 km. Additionally, sideband '−' tends to have comparable amplitudes to sideband '+' near 97 km and 105 km, but sideband '+' is largely absent near 220 km and 270 km.

As previously noted, sideband '−' has a period of about 1.5 days and zonal wave number -2, compared with sideband '+' that has period of about 0.75 days and zonal wave number -4. While DE3-UFKW nonlinear interactions probably occur at altitudes lower than 97 km, the vertical propagation of the sidebands may depend on zonal mean winds at altitudes below 97 km and between 105 km and 220 km. For DE3 and the UFKW that are eastward propagating waves, the frequency tends to be Doppler shifted to higher absolute values in regions of westward wind and to lower absolute values in regions of eastward wind (Forbes, 2000). Waves with larger Doppler-shifted frequency are less effectively damped than those with smaller Doppler-shifted frequency in regions where dissipation is important. As a result, waves tends to exhibit larger amplitudes where Doppler shifting to higher absolute frequencies occurs. In other words, in their vertical propagation waves can move from regions in which they are able to propagate through regions in which they are evanescent (process sometime referred to as wave tunneling). Regions of evanescence exist where the buoyancy frequency of the atmosphere is greater than the intrinsic frequency of a given wave, thus, it does not support buoyant motions when perturbed over those timescales. Regions of evanescence for waves that are able to propagate at other altitudes can occur via changes in the temperature of the atmosphere with altitude or by altitudinal changes in the wind. The altitude at which the buoyancy frequency matches the intrinsic frequency of the wave is known as reflection level. In addition to Doppler-shifting mean wind effects, generally higher zonal wave numbers correspond to shorter vertical wavelengths and hence more susceptibility to dissipation. Follow-on work will investigate in detail the height-latitude structure of primary waves and SWs in MIGHTI data to study their propagation characteristics.

The absence of a clear DE3 signature in thermospheric zonal winds near 270 km suggests that dissipation for this wave component may be occurring between 220 and 270 km. While greater middle thermospheric amplitudes for sideband '−' compared to sideband '+' may be due to a shorter vertical wavelength (higher zonal wave number) for sideband '+'. Based on the discussion above, this is latter finding is consistent with the higher zonal wave number for sideband '+'. The results in Figures 6 and 7 provide no conclusive explanation on why one sideband might be more readily excited than another, or why both might be excited during one period of time and not another, or why one might propagate to higher altitudes and the other not. The absence of DE3 and sideband '+' in MIGHTI zonal winds near 270 km is a strong indication that the DE3 and sideband '+' upper F-region ion density wave signatures observed by ICON and C2E2 IVM (i.e., Figures 6c and 6d) are likely to be primarily driven by E-region dynamo processes as opposed to direct F-region in-situ electro-dynamical coupling. Follow-on work will employ contemporaneous TIMED/SABER and SORTIE IVM observations to study in detail the

spatial and temporal variability associated with primary waves and SWs in the lower and middle atmosphere and mid-latitude F-region ionosphere.

Finally, the PL spectra shown in Figures 7a'-d' demonstrate large periodicities around 1 cycles that are significantly more prominent than those observed in upper F-region ion densities. These wave-1 variations are likely associated with the stationary planetary wave component of wavenumber 1 (SPW1) resulting from the offset between the geographic and geomagnetic fields, driven by ion-neutral interactions, in the E-region or lower F-region ionosphere. Forbes et al. (2009), Oberheide et al. (2011b), Forbes et al. (2012), Jones et al. (2013), among others, proposed that a plasma-neutral interaction due to the offset between the geographic and geomagnetic fields may be responsible for the in-situ generation of a number of non-migrating tidal components. In particular, Oberheide et al. (2011b) suggested that the D0 and DW2 could be generated via a non-linear interaction between the in-situ generated DW1 (via EUV solar radiation absorption) and the SPW1 resulting from the offset between the geographic and geomagnetic fields (driven by plasma-neutral interactions). All of these wave components are responsible for a wave-1 signature as viewed in a slowly-precessing orbit. Follow-on analyses of contemporaneous ICON MIGHTI and IVM measurements will cast new light into some of the questions raised by these studies on the origin of thermospheric wave-1 longitudinal variability.

6 Summary and Conclusions

Recent availability of critical parameters characterizing the IT from nearly coincident space-borne instruments offered the unique opportunity to investigate fundamental mechanisms responsible for coupling lower and middle thermospheric wind variability with F-region ion density variability via large-scale atmospheric wave propagation.

In this study, we first carried out comprehensive correlation analyses of in-situ ICON and C2E2 total ion densities centered around a 40-day period of similar MLT coverage extending from 11 July 2020 through 20 August 2020. These analyses demonstrated significant agreement between the ICON and C2E2 ion density measurements near 590 km and 540 km altitude, respectively. Pearson correlation coefficients were found to vary between r=0.631 and r=0.785, greatest between 13°N and 28°N MLAT, and generally higher during daytime in the southern hemisphere and nighttime in the northern hemisphere.

Next, we applied spectral analysis techniques to both ICON IVM and C2E2 IVM total ion densities to study the presence and impacts of global-scale waves on the upper F-region ionosphere at two altitudes separated by only about 50 km. Remarkable agreement was found between the ICON and C2E2 ion density spectra. Wave analyses revealed a rich spectrum of upward propagating global-scale waves, including large non-migrating diurnal DE3, DE2, and DE1 tidal

and 3-day UFKW variations, as well as prominent SWs associated with tidal-UFKW nonlinear interactions.

Finally, we applied the spectral analysis methods to concurrently remotely-sensed ICON MIGHTI zonal winds near 95-105 km and 220-270 km to study connections with the lower and middle thermosphere. The aim was to gain novel insights on the ability of the selected group of high-impact global-scale waves to propagate into the middle thermosphere and generate F-region ion density variability. This analysis demonstrated strong similarities between the concurrently-observed ionospheric and lower/middle thermospheric wave-induced variability. The thermospheric zonal wind spectra for 1-7 August 2020 were found to be dominated by DE3, the UFKW, and their sidebands with s = -2 and period of $\sim$0.75 day (sideband '$-$') and with s = -4 and period of $\sim$1.5 days (sideband '+'). The thermospheric DE3 was found to be larger near 105 km than $\sim$97 km, consistent with the vertical propagation and grown of this tidal component up to $\sim$110-120 km altitude. While present near 220 km with significantly reduced amplitudes, DE3 was found to be largely absent near 270 km. Sideband '$-$' was found to have comparable amplitudes to sideband '+' both near 97 km and 105 km, while sideband '+' was found to be negligible near 220 km and 270 km. For eastward-propagating waves, including the UFKW, DE3 and their two sidebands, the frequency is Doppler shifted to lower absolute values in regions of eastward mean winds, while higher zonal wave number waves are generally characterized by shorter vertical wavelengths. Both of these effects would correspond to greater susceptibility to molecular dissipation for these wave components. The absence of DE3 and sideband '+' in thermospheric zonal wind near 270 km suggests that the ionospheric signatures are likely to be primarily driven by E-region dynamo processes as opposed to direct F-region in-situ electro-dynamical coupling or compositional effects.

The results herein presented emphasize the importance of studying how and to what extent vertically-propagating global-scale waves originating in the lower and middle atmosphere contribute IT variability. Nonlinear interactions among these waves are shown to produce SWs that can be as large as the waves producing them. These findings indicate that nonlinear interactions involving global-scale waves are responsible for important variability that should be accounted for when analyzing IT variability in nonlinear models and satellite data. Follow-on work will study in detail the spatial and temporal variability in fundamental IT parameters associated with primary and SWs, including their overall impacts on day-to-day and spatial variability. These efforts will take advantage of contemporaneous and complementary ICON, COSMIC-2, SORTIE, and TIMED satellite observations and will include investigating the relative contribution of different processes for generating F-region ionospheric variability. MIGHTI wind observations will provide an excellent data set for investigating the height-latitude structures of primary waves and SWs as they propagate through the lower and middle thermosphere, while analyses of IVM data from the SORTIE CubeSat with an orbital inclination near $\sim$51.6° will prove essential to study wave propagation to middle latitude regions.

Acknowledgements ICON is supported by NASA's Explorers Program through contracts NNG12FA45C and NNG12FA42I. ICON data are processed in the ICON Science Data Center at UCB and available at *https* : *//icon.ssl.berkeley.edu/data/* and from NASA's Space Physics Data Facility (SPDF) at *https* : *//spdf.gsfc.nasa.gov/pub/data/icon/l*2/. This work is partly supported by NASA Grant Number 80NSSC22K0019 to Atmospheric & Space Technology Research Associates (ASTRA). Further information on the ICON IVM product can be found in NASA's SPDF ICON directory at */documentation/ICON_L*2 − 7_*IVM* − *A_v*05.*pdf*. This study employs post-processed COSMIC-2 E2 IVM L2 total ion density available via the public site at *https* : *//data.cosmic.ucar.edu/gnss*−*ro/cosmic*2/*postProc/level*2/.

References

1. Andrews, D. G., J. R. Holton, and C. B. Leovy (1987), Middle Atmospheric Dynamics, Academic Press, 489.
2. Chang, L. C., J.Y. Liu, and S. E. Palo (2011), Propagating planetary wave coupling in SABER MLT temperatures and GPS TEC during the 2005/2006 austral summer, J. Geophys. Res., 116, A10324, doi:10.1029/2011JA016687.
3. Chou M-Y, et al. (2021), Validation of FORMOSAT-7/COSMIC2 IVM ion density and TGRS orbit electron density, Terrestrial, Atmospheric and Oceanic Sciences, doi: 10.3319/TAO.2021.06.22.01.
4. Crowley, G., C. Fish, M. Pilinski, E. Stromberg et al. (2016), Scintillation Observations and Response of The Ionosphere to Electrodynamics (SORTIE), Proceedings of the 30th Annual AIAA/USU SmallSat Conference, paper: SSC16-VI-3.
5. Cullens, C.Y., Immel, T.J., Triplett, C.C., Wu, Y.J., England, S.L., Forbes, J.M. and Liu, G. (2020), Sensitivity study for ICON tidal analysis, Progress in Earth and Planetary Science, 7, 1-13, doi: 10.1186/s40645-020-00330-6.
6. Dhadly, M. S., Englert, C. R., Drob, D. P., Emmert, J. T., Niciejewski, R., and Zawdie, K. A. (2021), Comparison of ICON/MIGHTI and TIMED/TIDI Neutral Wind Measurements in the Lower Thermosphere, J. Geophys. Res., 126, e2021JA029904, doi:10.1029/2021JA029904.
7. Egito, F., Buriti, R.A., Fragoso Medeiros, A., Takahashi, H. (2018), Ultrafast kelvin waves in the MLT airglow and wind, and their interaction with the atmospheric tides, Ann. Geophys. 36, 231-241, doi:10.5194/angeo-36-231-2018.
8. England, S. L., T. J. Immel, J. D. Huba, M. E. Hagan, A. Maute, and R. DeMajistre (2010), Modeling of multiple effects of atmospheric tides on the ionosphere: An examination of possible coupling mechanisms responsible for the longitudinal structure of the equatorial ionosphere, J. Geophys. Res., 115, A05308, doi:10.1029/2009JA014894.
9. England, S. L. (2011), A review of the effects of non-migrating atmospheric tides on the Earth's low-latitude ionosphere, Space Sci. Rev., doi:10.1007/s11214-011-9842-4.
10. Englert, C. R., Harlander, J. M., Brown, C. M., and Marr, K. D. (2015), Spatial heterodyne spectroscopy at the Naval Research Laboratory, Applied Optics, 54(31), F158., doi:10.1364/ao.54.00f158.
11. Englert, C. R., Harlander, J. M., Brown, C. M., Marr, K. D., Miller, I. J., Stump, J. E., and Immel, T. J. (2017), Michelson Interferometer for global high-resolution thermospheric imaging (MIGHTI): Instrument design and calibration, Space Science Reviews, 212(1-2), 553-584, doi:10.1007/s11214-017-0358-4.
12. Englert, C. R., K. D. Marr, J. M. Harlander, and B.J. Harding (2022), Spatial Resolution of the MIGHTI Thermospheric Wind Measurements and Implications on Wind Shear Measurements, OSA Optical Sensors and Sensing Congress 2021, https://www.osapublishing.org/abstract.cfm?URI=FTS-2021-FTh4G.2.
13. Fejer, B. G. (1981), The equatorial ionospheric electric field. A review, J. Atm. Solar Terr. Phys., 43(5-6), 377-386, doi:10.1016/0021-9169(81)90101-X
14. Fejer, B. G. (2002), Low latitude storm time ionospheric electrodynamics, J. Atm. Solar Terr. Phys., 64(12-14), 1401-1408.
15. Forbes, J. M. (2000), Wave coupling between the lower and upper atmosphere: Case study of an ultra-fast Kelvin wave, J. Atm. Solar Terr. Phys., 62, 1603-1621.

16. Forbes, J. M. and D. Wu (2006), Solar Tides as Revealed by Measurements of Mesosphere Temperature by the MLS Experiment on UARS, J. Atmos. Sci., 63, 1776-1797.
17. Forbes, J. M., S. L. Bruinsma, X. Zhang, and J. Oberheide (2009), Surface-exosphere coupling due to thermal tides, Geophys. Res. Lett., 36, L15812, doi:10.1029/2009GL038748.
18. Forbes, Jeffrey M., Xiaoli Zhang, and Sean Bruinsma (2012), Middle and upper thermosphere density structures due to nonmigrating tides, J. Geophys. Res. Space Physics, 117, A11, doi:10.1029/2012JA018087.
19. Forbes, J. M., and Zhang, X. (2017), The quasi-6 day wave and its interactions with solar tides, J. Geophys. Res. Space Physics, 122, 4764-4776, doi:10.1002/2017JA023954.
20. Forbes, J.M., Zhang, X., Hagan, M.E., England, S.L., Liu, G. and Gasperini, F. (2017), On the Specification of Upward-Propagating Tides for ICON Science Investigations, Space Science Reviews, 212(1-2), 697-713, doi:10.1007/s11214-017-0401-5.
21. Forbes, J. M., Maute, A., Zhang, X., and Hagan, M. E. (2018), Oscillation of the ionosphere at planetary-wave periods, J. Geophys. Res. Space Physics, 123, 7634-7649, doi:10.1029/2018JA025720.
22. Forbes, J. M., He, M., Maute, A., and Zhang, X. (2020a), Ultrafast Kelvin wave variations in the surface magnetic field, J. Geophys. Res. Space Physics, 125, doi:10.1029/2020JA028488.
23. Forbes, J. M., Maute, A., and Zhang, X.(2020b), Dynamics and electrodynamics of an ultra-fast Kelvin wave (UFKW) packet in the ionosphere-thermosphere (IT), J. Geophys. Res. Space Physics, 125, doi:10.1029/2020JA027856.
24. Forbes, J. M., Zhang, X., and Maute, A. (2020c), Planetary wave (PW) generation in the thermosphere driven by the PW-modulated tidal spectrum, J. Geophys. Res. Space Physics, 125, doi:10.1029/2019JA027704.
25. Forbes, J.M., Heelis, R., Zhang, X., Englert, C.R., Harding, B.J., He, M., Chau, J.L., Stoneback, R., Harlander, J.M., Marr, K.D. and Makela, J.J., (2021a), Q2DW-tide and-ionosphere interactions as observed from ICON and ground-based radars, J. Geophys. Res. Space Physics, doi:10.1029/2021JA029961.
26. Forbes, J. M., Zhang, X., Heelis, R., Stoneback, R., Englert, C. R., Harlander, J. M., et al. (2021b), Atmosphere-Ionosphere (A-I) coupling as viewed by ICON: Day-to-day variability due to planetary wave (PW)-tide interactions, J. Geophys. Res. Space Physics, 126, doi:10.1029/2020JA028927.
27. Gan, Q., Oberheide, J., Yue, J., and Wang, W. (2017), Short-term variability in the ionosphere due to the nonlinear interaction between the 6 day wave and migrating tides, J. Geophys. Res. Space Physics, 122, 8831-8846, doi:10.1002/2017JA023947.
28. Gan, Q., Wang, W., Yue, J., Liu, H., Chang, L. C., Zhang, S., Burns, A., and Du, J. (2016), Numerical simulation of the 6 day wave effects on the ionosphere: Dynamo modulation, J. Geophys. Res. Space Physics, 121, 10103-10116, doi:10.1002/2016JA022907.
29. Gasperini, F., J. M. Forbes, E. N. Doornbos, and S. L. Bruinsma (2015), Wave coupling between the lower and middle thermosphere as viewed from TIMED and GOCE, J. Geophys. Res., 120, 5788-5804, doi:10.1002/2015JA021300.
30. Gasperini, F., Forbes, J. M., and Hagan, M. E. (2017a), Wave coupling from the lower to the middle thermosphere: Effects of mean winds and dissipation, J. Geophys. Res., 122, 7781-7797, doi:10.1002/2017JA024317.
31. Gasperini, F, M. E. Hagan, and Y. Zhao (2017b), Evidence of tropospheric 90-day oscillations in the thermosphere, Geophys. Res. Lett., doi:10.1002/2017GL075445.
32. Gasperini, F., Forbes, J. M., Doornbos, E. N., and Bruinsma, S. L. (2018), Kelvin wave coupling from TIMED and GOCE: Inter/intra-annual variability and solar activity effects, J. Atmos. Sol.-Terr. Phys., 171, 176-187, doi:10.1016/j.jastp.2017.08.034.
33. Gasperini, F., Liu, H., and McInerney, J. (2020), Preliminary evidence of Madden-Julian Oscillation effects on ultrafast tropical waves in the thermosphere, J. Geophys. Res., 125, e2019JA027649, doi:10.1029/2019JA027649.
34. Gasperini, F., Azeem, I., Crowley, G., Perdue, M., Depew, M., Immel, T., et al. (2021), Dynamical coupling between the low-latitude lower thermosphere and ionosphere via the non-migrating diurnal tide as revealed by concurrent satellite observations and numerical modeling., Geophys. Res. Lett., 48, e2021GL093277, doi:10.1029/2021GL093277.

35. Gu, S.-Y., Dou, X., Lei, J., Li, T., Luan, X., Wan, W., and Russell III, J. M. (2014a), Ionospheric response to the ultrafast Kelvin wave in the MLT region, J. Geophys. Res. Space Physics, 119, 1369-1380, doi:10.1002/2013JA019086.
36. Gu, S.-Y., Liu, H. L., Li, T., Dou, X. K., Wu, Q., and Russell, J. M. (2014b), Observation of the neutral-ion coupling through 6 day planetary wave, J. Geophys. Res. Space Physics, 119, 10376-10383, doi:10.1002/2014JA020530.
37. Gu, S.-Y., Ruan, H., Yang, C.-Y., Gan, Q., Dou, X., and Wang, N. (2018), The morphology of the 6-day wave in both the neutral atmosphere and F region ionosphere under solar minimum conditions, J. Geophys. Res. Space Physics, 123 (5), 4232-4240
38. Hagan, M. E. (1996), Comparative effects of migrating solar sources on tidal signatures in the middle and upper atmosphere, J. Geophys. Res., 101, 21213-21222.
39. Harding, B.J., Chau, J.L., He, M., Englert, C.R., Harlander, J.M., Marr, K.D., Makela, J.J., Clahsen, M., Li, G., Ratnam, M.V. and Bhaskar Rao, S.V. (2021), Validation of ICON-MIGHTI thermospheric wind observations: 2. Green-line comparisons to specular meteor radars, J. Geophys. Res. Space Physics, doi:10.1029/2020JA028947.
40. Harding, B.J., Makela, J.J., Englert, C.R., Marr, K.D., Harlander, J.M., England, S.L. and Immel, T.J. (2017), The MIGHTI Wind Retrieval Algorithm: Description and Verification, Space Science Reviews, 212(1-2), 585-600, doi:10.1007/s11214-017-0359-3.
41. He, M., L. Liu, W. Wan, and Y. Wei (2011), Strong evidence for couplings between the ionospheric wave-4 structure and atmospheric tides, Geophys. Res. Lett., 38, L14101, doi:10.1029/2011GL047855.
42. Heelis, R. A. (2004), Electrodynamics in the low and middle latitude ionosphere: A tutorial, J. Atm. Solar Terr. Phys., 66(10), 825-838.
43. Heelis, R.A., Stoneback, R.A., Perdue, M.D., Depew, M.D., Morgan, W.A., Mankey, M.W., Lippincott, C.R., Harmon, L.L., and Holt, B.J., (2017), Ion Velocity Measurements for the Ionospheric Connections Explorer, Sp. Sci. Rev., 212(1-2), 615-629, doi:10.1007/s11214-017-0383-3.
44. Huba, J. D., Heelis, R., and Maute, A. (2021), Large-scale O+ depletions observed by ICON in the post-midnight topside ionosphere: Data/model comparison, Geophy. Res. Lett., 48, e2020GL092061, doi:10.1029/2020GL092061.
45. Immel, T.J., England, S.L., Mende, S.B. et al. (2018), The Ionospheric Connection Explorer Mission: Mission Goals and Design, Sp. Sci. Rev. 214, 13, doi:10.1007/s11214-017-0449-2.
46. Immel, T.J. and Eastes, R.W. (2019), New NASA missions focus on terrestrial forcing of the space environment, Bull. Amer. Meteor. Soc., 100, 2153-2156, doi:10.1175/BAMS-D-19-0066.1
47. Immel, T. J., Harding, B. J., Heelis, R. A., Maute, A., Forbes, J. M., England, S. L., et al. (2021), Regulation of ionospheric plasma velocities by thermospheric winds, Nature Geoscience, 1-6, doi:10.1038/s41561-021-00848-4.
48. Jones, M., Forbes, J. M., Hagan, M. E., and Maute, A. (2013), Non-migrating tides in the ionosphere-thermosphere: In situ versus tropospheric sources, J. Geophys. Res. Space Physics, 118, 2438– 2451, doi:10.1002/jgra.50257.
49. Jones, M. Jr., J. M. Forbes, and M. E. Hagan (2014), Tidal-induced net transport effects on the oxygen distribution in the thermosphere, Geophys. Res. Lett., 41, GL060698.
50. Lieberman, R. S., Riggin, D. M., Ortland, D. A., Nesbitt, S. W., and Vincent, R. A. (2007), Variability of mesospheric diurnal tides and tropospheric diurnal heating during 1997-1998, J. Geophys. Res., 112, D20110, doi:10.1029/2007JD008578.
51. Lieberman, R. S. (1991), Nonmigrating diurnal tides in the equatorial middle atmosphere, J. Atmos. Sci., 48, 1112 - 1123.
52. Lin, C.-Y., Lin, C. C.-H., Liu, J.-Y., Rajesh, P. K., Matsuo, T., Chou, M.-Y., et al. (2020), The early results and validation of FORMOSAT-7/COSMIC-2 space weather products: Global ionospheric specification and Ne-aided Abel electron density profile, J. Geophys. Res. Space Physics, 125, doi:10.1029/2020JA028028.
53. Liu, H.-L., V. A. Yudin, and R. G. Roble, Day-to-day ionospheric variability due to lower atmosphere perturbations (2013), Geophys. Res. Lett., 40, 665-670, doi:10.1002/grl.50125.
54. Liu, H. -L. (2016), Variability and predictability of the space environment as related to lower atmosphere forcing, Space Weather, 14, 634-658, doi:10.1002/2016SW001450.

55. Liu, G., England, S.L., Lin, C.S., Pedatella, N.M., Klenzing, J.H., Englert, C.R., Harding, B.J., Immel, T.J. and Rowland, D.E. (2021), Evaluation of Atmospheric 3-Day Waves as a Source of Day-to-Day Variation of the Ionospheric Longitudinal Structure, Geophys. Res. Lett., 48(15), doi:10.1029/2021GL094877.
56. Makela, J.J., Baughman, M., Navarro, L.A., Harding, B.J., Englert, C.R., Harlander, J.M., Marr, K.D., Benkhaldoun, Z., Kaab, M. and Immel, T.J. (2021), Validation of ICON-MIGHTI thermospheric wind observations: 1. Nighttime Red-line Ground-Based Fabry-Perot Interferometers, J. Geophys. Res. Space Physics, doi:10.1029/2020JA028726.
57. Miyoshi, Y., and Yamazaki, Y. (2020), Excitation mechanism of ionospheric 6-day oscillation during the 2019 September sudden stratospheric warming event, J. Geophys. Res. Space Physics, 125, e2020JA028283, doi:10.1029/2020JA028283.
58. Moudden, Y., and J.M. Forbes (2010), A new interpretation of Mars aerobraking variability: Planetary wave-tide interactions, J. Geophys. Res., 115, E09005, doi:10.1029/2009JE003542.
59. Moudden, Y., and J. M. Forbes (2011), First detection of wave interactions in the middle atmosphere of Mars, Geophys. Res . Lett., 38, L04202, doi:10.1029/2010GL045592.
60. Moudden, Y., and J.M. Forbes (2013), A decade-long climatology of terdiurnal tides using TIMED/SABER observations, J. Geophys. Res., 118, 4534-4550, doi:10.1002/jgra.50273.
61. Moudden, Y., and J. M. Forbes (2014), Quasi-two-day wave structure, interannual variability, and tidal interactions during the 2002-2011 decade, J. Geophys. Res. Atmos., 119, 2241-2260, doi:10.1002/2013JD020563.
62. Oberheide, J., and Gusev, O. A. (2002), Observation of migrating and nonmigrating diurnal tides in the equatorial lower thermosphere, Geophys. Res. Lett., 29(24), 2167, doi:10.1029/2002GL016213.
63. Oberheide, J., Q. Wu, T. L. Killeen, M. E. Hagan, and R. G. Roble (2006), Diurnal nonmigrating tides from TIMED Doppler Interferometer wind data: Monthly climatologies and seasonal variations, J. Geophys. Res., 111, A10S03, doi:10.1029/2005JA011491.
64. Oberheide, J., J. M. Forbes, X. Zhang, and S. L. Bruinsma (2011a), Wave-driven variability in the ionosphere- thermosphere-mesosphere system from TIMED observations: What contributes to the 'wave 4'?, J. Geophys. Res., 116, A01306, doi:10.1029/2010JA015911.
65. Oberheide, J., Forbes, J. M., Zhang, X., and Bruinsma, S. L. (2011b), Climatology of upward propagating diurnal and semidiurnal tides in the thermosphere, J. Geophys. Res., 116, A11306, doi:10.1029/2011JA016784.
66. Oberheide, J., J. Forbes, K. Hausler, Q. Wu, and S. L. Bruinsma (2009), Tropospheric tides from 80-400 km: Propagation, inter-annual variabil- ity and solar cycle effects, J. Geophys. Res., doi:10.1029/2009JD012388.
67. Palo, S. E., R. G. Roble, and M. E. Hagan (1999), Simulation of the quasi-two-day wave using the TIME-GCM: Dynamical effects in the middle atmosphere, Earth Planets Space, 51, 629-647.
68. Park, J., Heelis, R. and Chao, C.K., (2021a), Ion velocity and temperature variation around topside nighttime irregularities: Contrast between low-and mid-latitude regions, J. Geophys. Res. Space Physics, 126(2), doi:10.1029/2020JA028810.
69. Park, J., Huba, J. D., Heelis, R., and Englert, C. (2021b), Isolated peak of oxygen ion fraction in the post-noon equatorial F-region: ICON and SAMI3/WACCM-X, J. Geophys. Res. Space Physics, 126, doi:10.1029/2021JA029217.
70. Pedatella, N. M., and J. M. Forbes (2009), Interannual variability in the longitudinal structure of the low-latitude ionosphere due to the El Niño–Southern Oscillation, J. Geophys. Res., 114, A12316, doi:10.1029/2009JA014494.
71. Salby, M. L., D. L. Hartmann, P. L. Bailey, and J. C. Gille (1984), Evidence for equatorial Kelvin modes in Nimbus-7 LIMS, J. Atmos. Sci., 41, 220-235.
72. Schreiner, W. S., Weiss, J. P., Anthes, R. A., Braun, J., Chu, V., Fong, J., et al. (2020), COSMIC-2 radio occultation constellation: First results, Geophy. Res. Lett., 47, doi:10.1029/2019GL086841.
73. Triplett, C.C., Immel, T.J., Wu, Y.J. and Cullens, C. (2019), Variations in the ionosphere-thermosphere system from tides, ultra-fast Kelvin waves, and their interactions, Adv. Sp. Res., 64(10), 1841-1853, doi:10.1016/j.asr.2019.08.015.

74. Truskowski, A.O., Forbes, J.M., Zhang, X., and S.E. Palo (2014), New perspectives on thermosphere tides - 1. Lower thermosphere spectra and seasonal-latitudinal structures, Earth, Planets and Space, 66-136, doi:10.1186/s40623-014-0136-4.
75. Vanicek, P. (1969), Approximate spectral analysis by least-squares fit, Astrophys. Space Sci., 4, 387–391.
76. Vanicek, P. (1971), Further development and properties of the spectral analysis by least-squares, Astrophys. Space Sci., 12, 10–33.
77. Yamazaki, Y., and Miyoshi, Y. (2021), Ionospheric signatures of secondary waves from quasi-6-day wave and tide interactions. J. Geophys. Res. Space Physics, 126, doi:10.1029/2020JA028360.
78. Yamazaki, Y., Arras, C., Andoh, S., Miyoshi, Y., Shinagawa, H., Harding, B.J., Englert, C.R., Immel, T.J., Sobhkhiz-Miandehi, S. and Stolle, C. (2022), Examining the Wind Shear Theory of Sporadic E with ICON/MIGHTI Winds and COSMIC-2 Radio Occultation Data, Geophy. Res. Lett., doi:10.1029/2021GL096202.
79. Yigit, E., and A. S. Medvedev (2015), Internal wave coupling processes in Earth's atmosphere, Adv. Space Res., 55, 983-1003.
80. Yue, J., and Wang, W. (2014), Changes of thermospheric composition and ionospheric density caused by quasi 2 day wave dissipation, J. Geophys. Res. Space Physics, 119, 2069-2078, doi:10.1002/2013JA019725.
81. Zhang, X., J. M. Forbes, M. E. Hagan, J. M. Russell III, S. E. Palo, C. J. Mertens, and M. G. Mlynczak (2006), Monthly tidal temperatures 20-120 km from TIMED/SABER, J. Geophys. Res., 111, A10S08, doi:10.1029/2005JA011504.

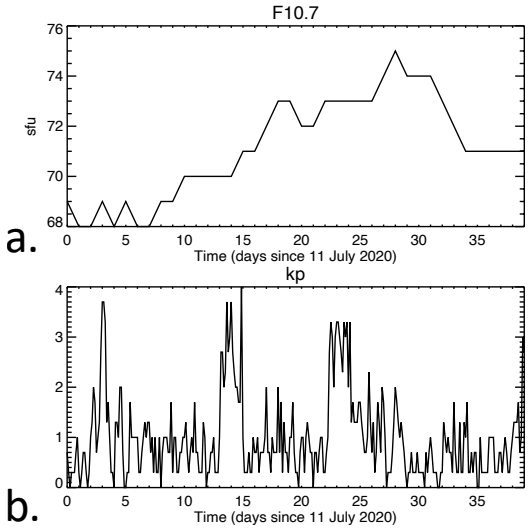

Fig. 1 Time series of the daily F10.7 solar flux (panel a) and 3-hourly Kp geomagnetic (panel b) indices during 11 July 2020 - 20 August 2020.

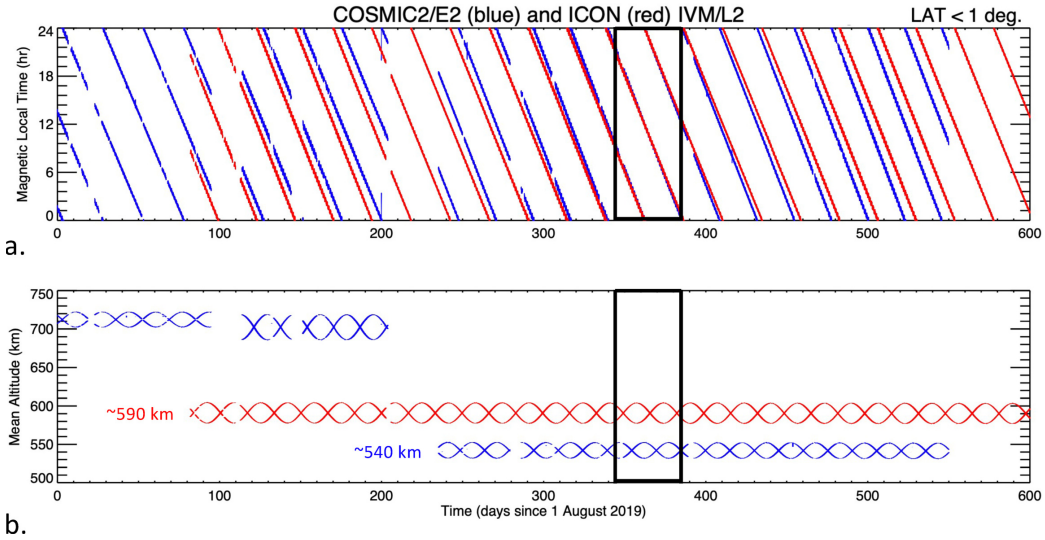

Fig. 2 Time series of equatorial C2E2 (blue) and ICON (red) magnetic local time (MLT) (panel a) and mean altitude (panel b) from 1 August 2019 through 23 March 2021. The black box denotes the 40-day period between 11 July 2020 and 20 August 2020 with similar (within about 30-min) MLT focus of this study.

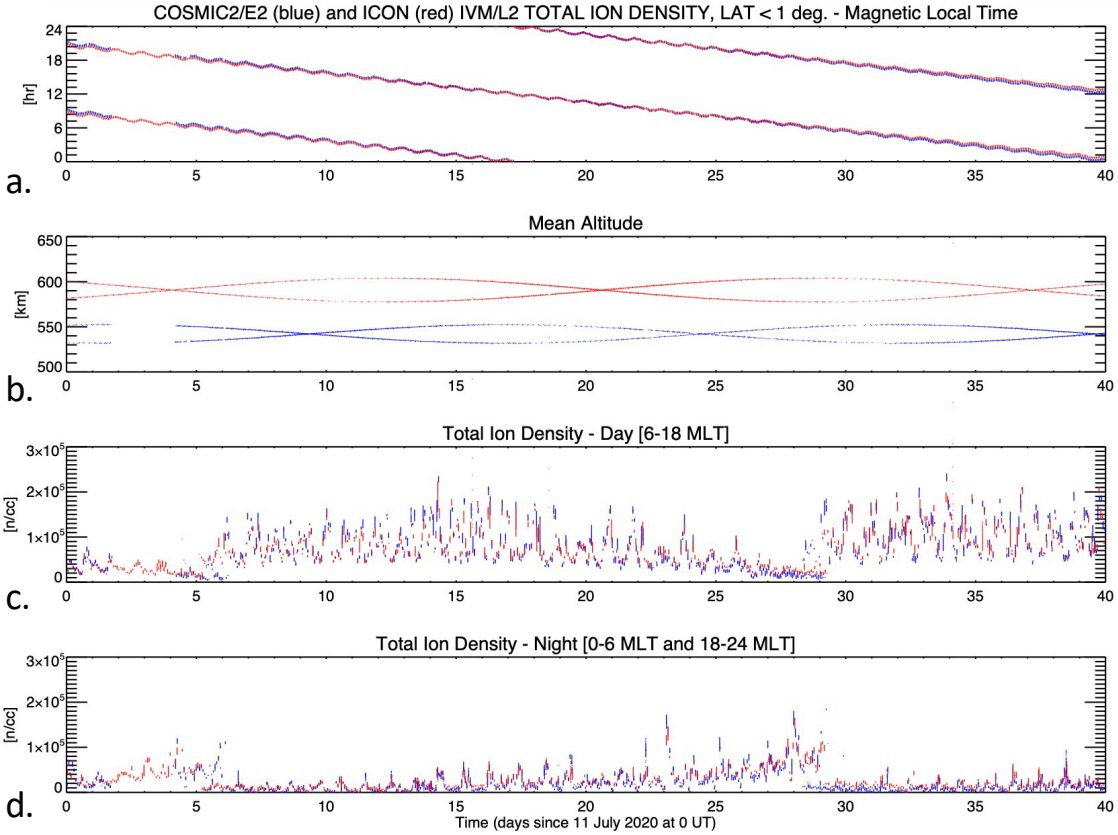

Fig. 3 Time series of C2E2 (blue) and ICON (red) MLT (panel a), mean altitude (panel b), daytime (6-18 MLT, panel c) and nighttime (0-6 MLT and 18-24 MLT, panel d) total ion densities during 11 July 2020 - 20 August 2020 near the geomagnetic equator.

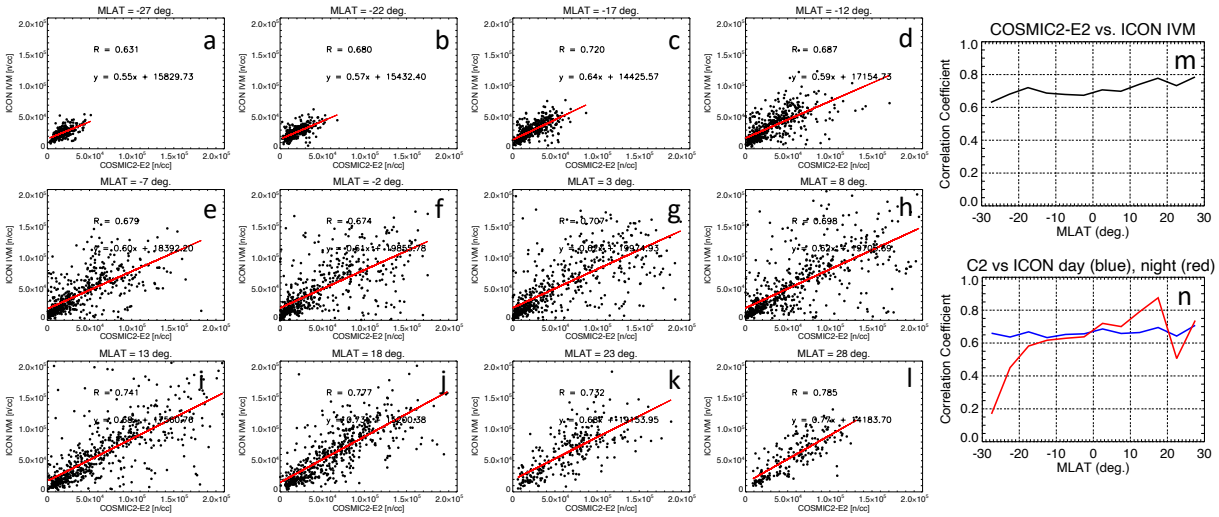

Fig. 4 Scatter plots of ICON versus C2E2 total ion densities from 27°S to 28°N MLAT in 5° bins (panels a-l). Fitting line (shown in red), fitting coefficient, and Pearson correlation coefficients also included in each panel. The Pearson correlation coefficient computed as a function of MLAT for combined daytime/nighttime data (panel m) and for daytime (blue) and nighttime (red) data binned separately (panel n) are also included.

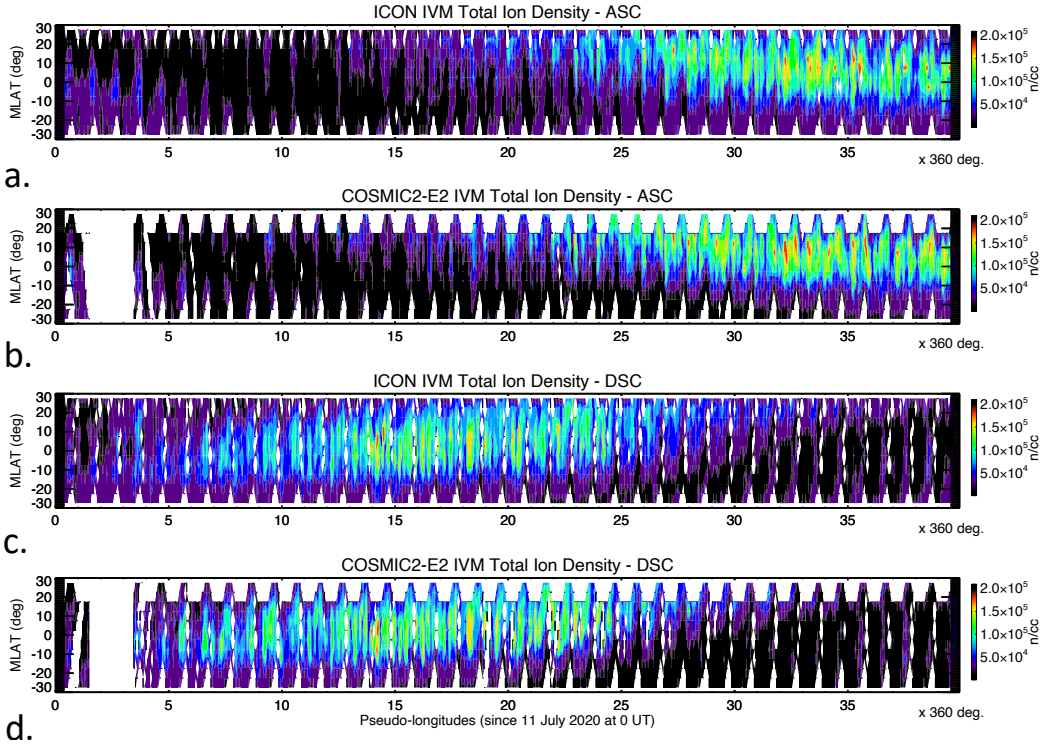

Fig. 5 MLAT versus pseudo-longitude structure of ascending and descending node ICON (panels a and c) and C2E2 (panels b and d) IVM total ion densities during 11 July 2020 - 20 August 2020.

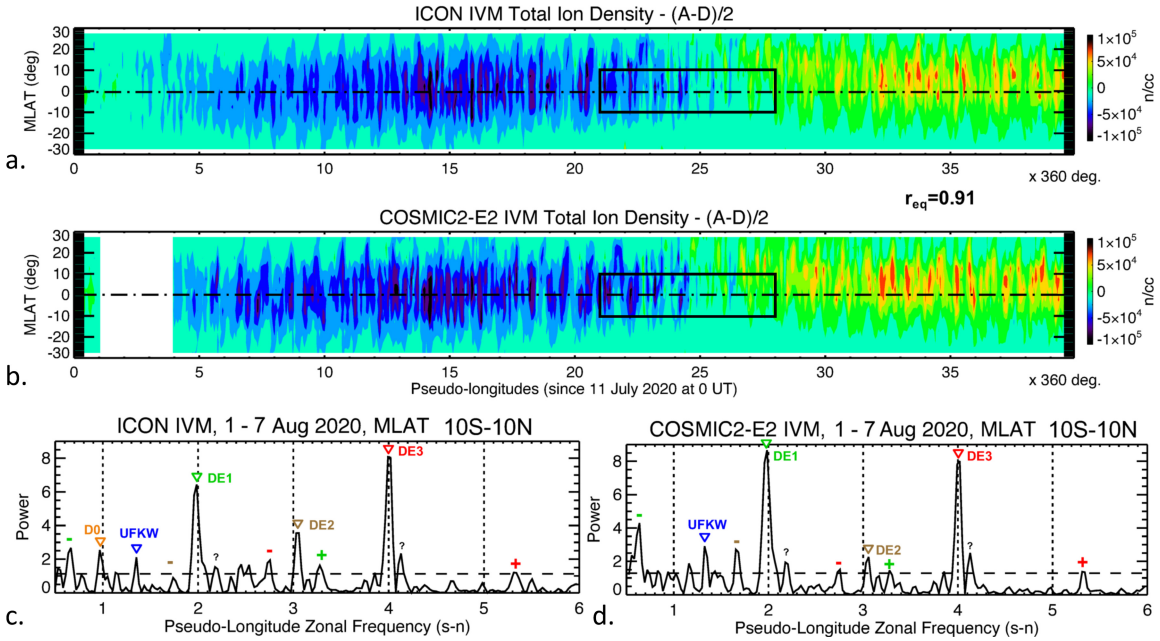

Fig. 6 MLAT versus pseudo-longitude contours of ICON (panel *a*) and C2E2 (panel *b*) IVM total ion density ascending/descending node differences (divided by 2) during 11 July 2020 - 20 August 2020. The white space in panel *b* denotes missing data for C2E2. The Pearson correlation coefficient between the ±10° MLAT averaged ICON and C2E2 ADND is calculated to be r=0.91, as noted at the bottom of panel a. Panels *c* and *d* contain the low-latitude (±10° MLAT) ICON and C2E2 spectra during 1-7 August 2020, respectively. Clearly marked in panels *c* and *d* are the wave components responsible the observed periodicities. The 'plus' and 'minus' symbols in panels *c* and *d* denote secondary waves due to tide-UFKW interactions. The black box in panels *a*-*b* denote the approximate data range used for the periodograms in panels *c*-*d*.

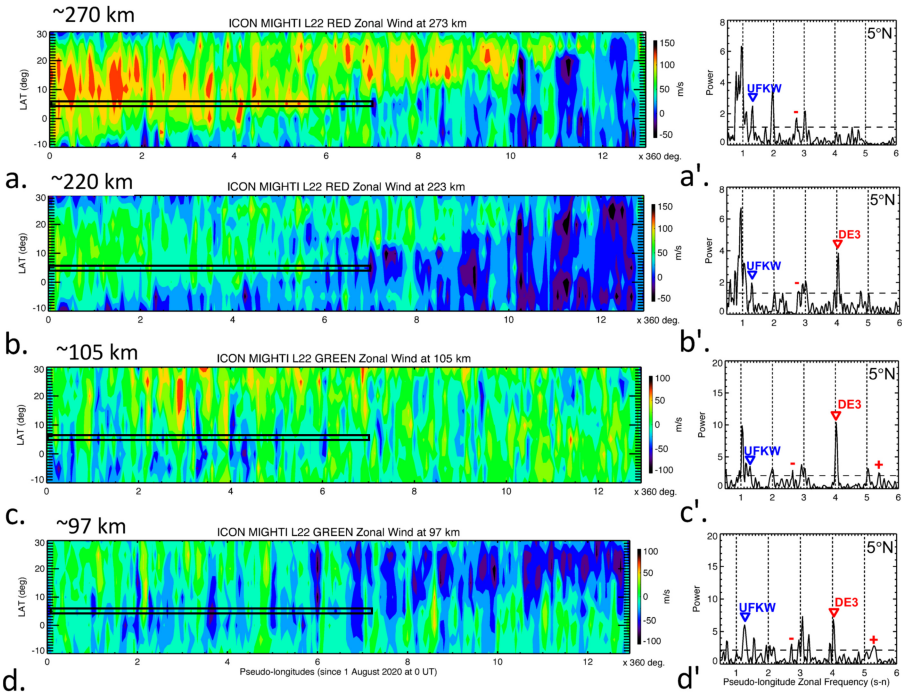

Fig. 7 Geographic latitude versus pseudo-longitude contours of ICON MIGHTI zonal wind ADND during 1 - 13 August 2020 near 270 km (panel *a*), 220 km (panel *b*), 105 km (panel *c*), and 97 km (panel *d*). Panels a'-d'contain the spectra computed at 5°N geographic latitude during 1-7 August 2020. Periodicities associated with a 3-day UFKW near 1.3 cycles (blue 'Δ' symbols), DE3 at 4 cycles (red 'Δ' symbols), and their two sidebands near 2.7 and 5.3 cycles (red 'minus' and 'plus' symbols) are clearly marked. The black box in panels *a*-*d* denote the approximate data range used for the periodograms in panels a'-d'.